Soft x-ray spectroscopy and microspectroscopy of correlated materials: photoemission and magnetic circular dichroism

2007 J. Phys.: Condens. Matter 19 125204

(http://iopscience.iop.org/0953-8984/19/12/125204)

IOP PUBLISHING JOURNAL OF PHYSICS: CONDENSED MATTER

J. Phys.: Condens. Matter **19** (2007) 125204 (26pp) doi:10.1088/0953-8984/19/12/125204

Soft x-ray spectroscopy and microspectroscopy of correlated materials: photoemission and magnetic circular dichroism

S Imada[1], **A Sekiyama and S Suga**

Graduate School of Engineering Science, Osaka University, 1-3 Machikaneyama, Toyonaka 560-8531, Japan

E-mail: imada@mp.es.osaka-u.ac.jp

Received 2 January 2007
Published 6 March 2007
Online at stacks.iop.org/JPhysCM/19/125204

Abstract

Spectroscopy and microspectroscopy of strongly correlated systems, ferromagnetic materials and magnetic microstructures by means of photoemission and magnetic circular dichroism using soft x-rays are presented. Bulk-sensitive high-resolution soft x-ray photoemission has revealed the real bulk electronic states of rare-earth compounds with various degrees of electronic correlation. Soft x-ray magnetic circular dichroism (XMCD) has enabled element-specific measurements of the system dependence of the orbital contribution to the magnetic moment, which has been shown to be enhanced when the magnetic electrons are more localized. XMCD microspectroscopy has been carried out for magnetic microstructures, which, by fully utilizing the spectroscopic aspect, has yielded not only the magnetic domain structures but also the distribution of the spin and orbital magnetic moment.

1. Introduction

Strong high-resolution soft x-rays have recently become available. This has, for the first time, allowed us to carry out not only bulk-sensitive high-resolution photoemission of strongly correlated electronic states, but also to carry out soft x-ray magnetic circular dichroism (XMCD) microspectroscopy of magnetic microstructures.

In section 2 there are reviewed the high-resolution bulk-sensitive photoemission studies of strongly correlated Ce and Pr compounds. These studies have revealed how the 4f excitation spectrum reflects the 4f electronic states, which range from localized to itinerant. In section 3, XMCD studies of ferromagnetic transition metal compounds are first presented focusing on the orbital contribution to the magnetic moment. Finally, XMCD microspectroscopic studies not

[1] Author to whom any correspondence should be addressed.

only of the domain structures of the magnetic microstructures but also of the electronic states across the spin reorientation transition in an epitaxial ferromagnetic double layer are presented.

2. Bulk-sensitive photoemission of strongly correlated materials

The electronic structure of the bulk is a crucial key for understanding the mechanism of various physical properties of strongly correlated materials. In this section are presented our studies on the bulk electronic structures of strongly correlated Ce and Pr compounds by means of bulk-sensitive high-resolution photoemission [1–5]. Bulk sensitivity is especially needed in rare-earth compounds since the valence number of the rare-earth ion is usually different between the surface and the bulk. Competition between localized and itinerant characters, which is the very origin of the strong correlation, has been found to be reflected clearly in the photoemission spectrum.

2.1. High-resolution bulk-sensitive photoemission

High-resolution bulk-sensitive photoemission has become possible by the recent development of the high-resolution soft x-ray beamline BL25SU at SPring-8 equipped with a state-of-the-art electron energy analyser. Bulk sensitivity owes to the use soft x-rays with photon energy ($h\nu$) typically in the range between 500 and 1500 eV. High energy resolution, which can be set as good as 50–100 meV, owes to the high brilliance, i.e. large photon number per unit energy width of the light source, and the high-resolution monochromator.

Photoemission, in which electrons emitted from the sample are detected while it is irradiated by photons, has been utilized as a powerful tool to elucidate the electronic structure. However, it has been impossible, until recently, to achieve good energy resolution in the bulk-sensitive photoemission due to the following reasons.

(a) The escape depth of the photoelectron from the solid surface depends drastically upon its kinetic energy, E_K [6]. Although this dependence depends very much upon material, the mean trend is that the escape depth is larger than ∼15 Å only if E_K is larger than ∼500 eV or smaller than ∼6 eV. When the electronic structure near the Fermi level E_F is studied, photon energy is about $E_K \sim h\nu - \phi$ where $h\nu$ is the photon energy and ϕ is the work function of the sample. Therefore, it should be necessary to use photon energy larger that ∼500 eV or smaller than ∼10 eV.

(b) On the other hand, development of high-resolution photoemission was historically first achieved in the $h\nu$ region between ∼20 and ∼100 eV, in which photoemission is very much surface sensitive. This might be due to the availability of high energy resolution in both the light source and the electron energy analyser. Total resolving power $E/\Delta E$ of 1000 already yields energy resolution better than 100 meV in this energy region.

Difficulty of achieving high resolution for $h\nu > 500$ eV comes from the fact that much higher resolving power is needed. For example, $E/\Delta E = 10\,000$ is needed to obtain resolution of 100 meV at $h\nu = 1000$ eV. In fact, state-of-the-art resolution had been 300 meV for $h\nu \sim$ 1000–1500 eV. Photoemission in the $h\nu$ region lower than 10 eV, on the other hand, had not been developed until recently presumably because people thought it inconvenient that the available energy range is very small. It should be noted that photoemission with $h\nu < 10$ eV is recently attracting much attention.

The beamline BL25SU at SPring-8 has been designed and constructed for soft x-ray spectroscopy, including photoemission, soft x-ray magnetic circular dichroism and microspectroscopy [9]. The light source is the twin helical undulator, through which the

8 GeV accumulated electrons travels and emit high-brilliance soft x-rays tunable in the energy range roughly between 200 and 3000 eV. A grazing incidence monochromator that employs varied-line-spacing plane gratings monochromatize photons roughly between 200 and 2000 eV. Photoelectrons are detected using a hemispherical electron energy analyser, SCIENTA SES-200. By the combination of these apparatuses, photoemission with unprecedented high total energy resolution of ∼100 meV at $h\nu \sim 1000$ eV has become possible.

2.2. Evolution of Ce 4f electronic structure from localized to itinerant character

Strongly correlated electronic states of many Ce, Sm, Yb and U compounds are considered to be due to the finite itinerancy of the electrons in the f shell, which is in the first approximation a core level. There have been found a wide range of Ce compounds, from those with nearly completely localized Ce 4f electrons to those with very much itinerant 4f electrons.

When the 4f electrons' itinerancy is moderate, the temperature dependence of the 4f electronic states is characterized by two crossover temperatures, namely, the Kondo temperature T_K and the coherent temperature T_{coh}, where $T_K > T_{coh}$. In the temperature range of $T > T_K$, each Ce atom acts as a thermally fluctuating local magnetic moment. For $T_K > T > T_{coh}$, the 4f electron and the conduction electrons couple and form a Kondo singlet at each Ce site, which causes the Kondo effect of electric resistance. For $T < T_{coh}$, coherence is developed in the hybridized state of Ce 4f electrons and the conduction electrons, which leads to the heavy fermion character. This is called 'the Kondo regime'.

When the 4f electrons' itinerancy is very strong, T_{coh} is higher than the room temperature and T_K is too high to be detected by usual experiments. Well hybridized states of 4f and the surrounding orbitals lead to strongly correlated valence and conduction electrons.

On the other hand, when the 4f electrons' itinerancy is weak enough, T_K is lower than the characteristic temperature of the RKKY intersite magnetic coupling. For such a system, T_K only has a virtual meaning and the Ce atoms act as local moments all the way down to a magnetic transition temperature T_M, below which the local magnetic moments order. This is called the 'RKKY regime'.

One should note that the crossover between the Kondo regime and the RKKY regime has recently attracted much attention. It is expected that both T_K and T_M becomes 0 K just at the crossover point, called 'the quantum critical point'. Non-Fermi liquid behaviour and superconductivity have been observed for such systems in the vicinity of the quantum critical point.

In order to extract the Ce 4f electronic structures of a Ce compound by means of photoemission, it is necessary to utilize a condition where the Ce 4f excitation is enhanced. Three such conditions has been known and utilized, namely, (A) Ce 4f state is enhanced at $h\nu = 40.8$ eV (He II) excitation compared to 21.2 eV (He I), (B) it is enhanced at the Ce 4d → 4f photoabsorption region ($h\nu \sim 122$ eV) compared to $h\nu$ just below the absorption threshold, which is called Ce 4d → 4f resonance photoemission (RPES) and (C) it is enhanced at the Ce 3d → 4f photoabsorption region ($h\nu \sim 882$ eV) again compared to just below the threshold, called Ce 3d → 4f RPES. Many high-resolution measurements under (A) and (B) had been performed but, as discussed above, the obtained spectra had probed mainly the surface region of Ce compounds.

In fact, qualitative difference was already found in measurements with moderate resolution under the much more bulk-sensitive condition (C), which revealed that the surface electronic states of Ce compounds are much different from the bulk one [7, 8]. In this section, we review the results of high-resolution Ce 3d → 4f RPES, which made the system dependence of the Ce 4f electronic structure much clearer than ever.

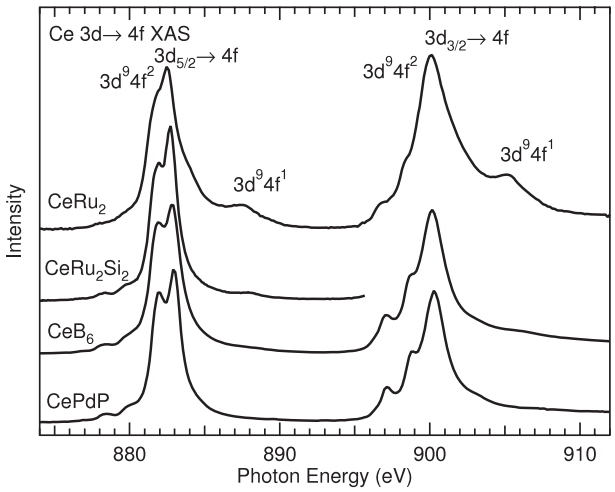

Figure 1. Ce 3d → 4f XAS for Ce compounds from localized to itinerant Ce 4f electrons.

Ce 3d → 4f photoabsorption spectra (XAS) of $CeRu_2$, $CeRu_2Si_2$, CeB_6 and CePdP are shown in figure 1. The character of the Ce 4f electron in these compounds span from itinerant to localized. $CeRu_2$ is a valence fluctuating superconductor in which the 4f electrons are considered to be fairly itinerant with T_K of the order of 1000 K. $CeRu_2Si_2$ and CeB_6 are considered to be Kondo materials with T_K of about 20 and 3 K, respectively. CePdP is a ferromagnet with $T_C = 5.2$ K where the localized Ce 4f moments are ordered.

Ce 3d → 4f XAS is split into two parts, namely, $h\nu$ region below 895 eV and that above it due to the strong spin–orbit interaction of the 3d core level. The former originates mainly from the electron excitation from the $j = 5/2$ state of the 3d core ($3d_{5/2}$ state) to the 4f level, and the latter from the $3d_{3/2} \rightarrow 4f$ excitation. In each of $3d_{5/2} \rightarrow 4f$ and $3d_{3/2} \rightarrow 4f$ regions, many structures are found. The structures found for CePdP corresponds quite well to the energy levels of $3d^9 4f^2$ configuration and the intensity distribution is well reproduced by the electric dipole transition from the $J = 5/2$ ground state of $4f^1$ to the $3d^9 4f^2$ final states [10]. This is consistent with the nearly localized character of the Ce 4f electrons in CePdP. On the other hand, prominent satellite structures are found for $CeRu_2$ at around 888 and 905 eV. These structures were found to have a $3d^9 4f^1$ character which appear when the ground state was taken as a mixture of $4f^0$ and $4f^1$ states [11]. This is consistent with the mixed valence 4f character of $CeRu_2$. Small but finite $3d^9 4f^1$ structures are also found for $CeRu_2Si_2$ and CeB_6, which is consistent with the Kondo character due to the finite hybridization between the Ce 4f state and the conduction band.

Ce 3d → 4f RPES consists of two photoemission spectra, one is the off-resonance spectrum taken at an $h\nu$ below any structure of 3d → 4f XAS and another is the on-resonance spectrum taken at an $h\nu$ where the 3d → 4f XAS intensity is large enough. Usually, the $h\nu$ for the on-resonance spectrum is set to the lowest prominent peak in order to avoid the possible extra structures in the spectrum due to an energy-loss process. We set the on-resonance $h\nu$ at about 882 eV and it has been found that the spectral shape does not change qualitatively in the ∼1 eV energy range about this $h\nu$. The $h\nu$ for the off-resonance spectrum is set to about 875 eV.

The 3d → 4f RPES spectra in the whole valence band region for the four Ce compounds are shown in figure 2. For each compound, on- and off-resonance spectra are normalized to each

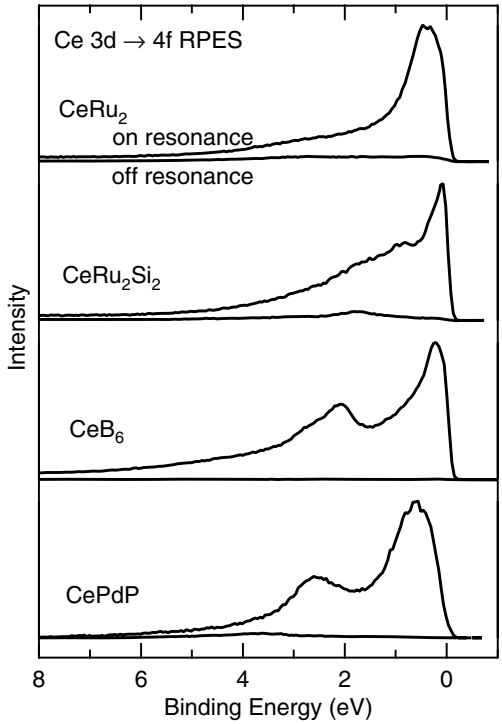

Figure 2. Ce 3d → 4f RPES of Ce compounds. The on-resonance spectrum and the off-resonance spectrum are normalized to each other by the photon number. The off- and on-resonance spectrum were taken at ∼875 and ∼882 eV, respectively.

other by dividing the spectra with the photon intensity. One can notice the strong enhancement of the spectral intensity due to the Ce 3d → 4f excitation. The enhancement is mainly due to the process

$$3d^{10}4f^{n} + h\nu \rightarrow 3d^{9}4f^{n+1} \rightarrow 3d^{10}4f^{n-1} + \text{photoelectron}. \quad (1)$$

This process is nearly equivalent to exciting 4f electron selectively out of all valence electrons. Therefore, the difference between the on-resonance and off-resonance spectra can be assumed to correspond mainly [12] to the Ce 4f excitation spectrum.

The bulk-sensitive Ce 4f excitation spectra obtained by Ce 3d → 4f RPES (dotted curves) are shown in figure 3 together with the surface-sensitive spectra obtained by 4d → 4f RPES (solid curves). The latter was obtained from on- and off-resonance spectra taken at ∼122 and ∼114 eV, respectively. For all the four compounds, it is clear that the bulk-sensitive spectrum is qualitatively different from the surface-sensitive one, which reconfirms the prominent difference of the Ce 4f state between the bulk and the surface.

Most of the 4f spectra are characterized by a structure between E_F and binding energy (E_B) of 1 eV and another structure between $E_B = 1.5$ and 3.5 eV, the latter being indicated by the vertical bars. The former (latter) structure has been attributed to the well (poorly) screened final state with approximately $4f^1$ ($4f^0$) configuration. More accurately, the well (poorly) screened final state is the bonding (antibonding) state of the $4f^1$ and $4f^0$ states that hybridize with each other in the final state but it is true that it has more $4f^1$ ($4f^0$) configuration.

For CeB_6 and CePdP, the bulk-sensitive 4f spectrum and the surface-sensitive one both have structures that are well and poorly screened. If we consider, as the first approximation,

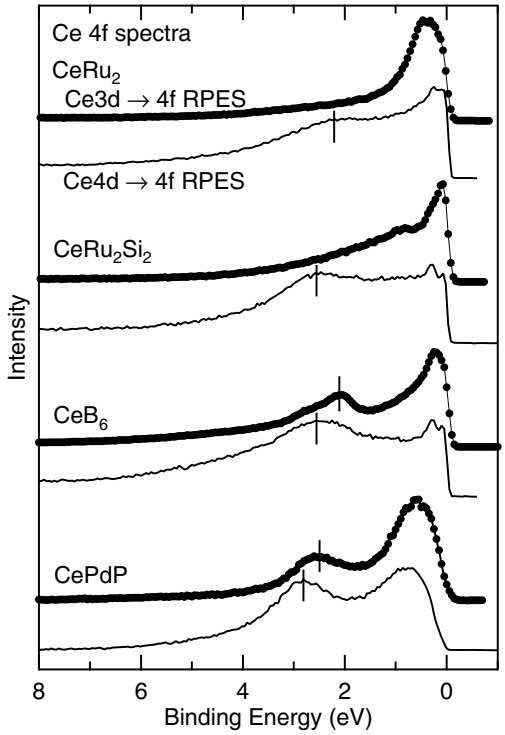

Figure 3. Bulk- and surface-sensitive Ce 4f spectra obtained by subtracting the off-resonance spectrum from the on-resonance spectrum of the Ce 3d → 4f and 4d → 4f RPES, respectively. The vertical bar represents the poorly screened peak and the structure just below E_F is the well screened peak.

the E_B of the poorly screened structure is the E_B of the bare 4f level, ε_f, it is seen from the spectra that ε_f at the surface of the sample is larger than that of the bulk by 0.4 eV in CeB_6 and by 0.3 eV in CePdP. For CePdP, more detailed study based on single impurity Anderson model has shown that the difference is much larger and ε_f of surface is larger by about 0.9 eV than the bulk [3]. The poorly screened structure of the bulk-sensitive 4f spectrum of $CeRu_2Si_2$ is considered to be present as a broad tail between about 1 and 3 eV. However, in the case of $CeRu_2$, the poorly screened structure is nearly smeared out in the bulk-sensitive 4f spectrum although it is found in the surface-sensitive spectrum.

One should note in figure 3 that the surface-sensitive 4f spectra of $CeRu_2$, $CeRu_2Si_2$ and CeB_6 are less different from each other than the bulk-sensitive ones. This is more drastically seen in the high-resolution (better than 100 meV) measurements near E_F shown in figure 4. For all the three compounds, the surface-sensitive Ce 4f spectrum obtained by the Ce 4d → 4f RPES has two peaks, one just below E_F and another between 200 and 300 meV and the intensity ratio does not change much. In the case of the bulk-sensitive 4f spectrum (3d → 4f RPES), such double-peak structure is found for CeB_6 but the near-E_F structure grows drastically in $CeRu_2Si_2$. Moreover, that for $CeRu_2$ has a qualitatively different line shape with a broad peak at around 400 meV and a hump at around 80 meV.

The small system dependence of the Ce 4f spectrum was one of the most puzzling results of the low-energy photoemission, namely, photoemission spectra of compounds with very different Ce 4f character looked very much alike. The present high-resolution bulk-sensitive

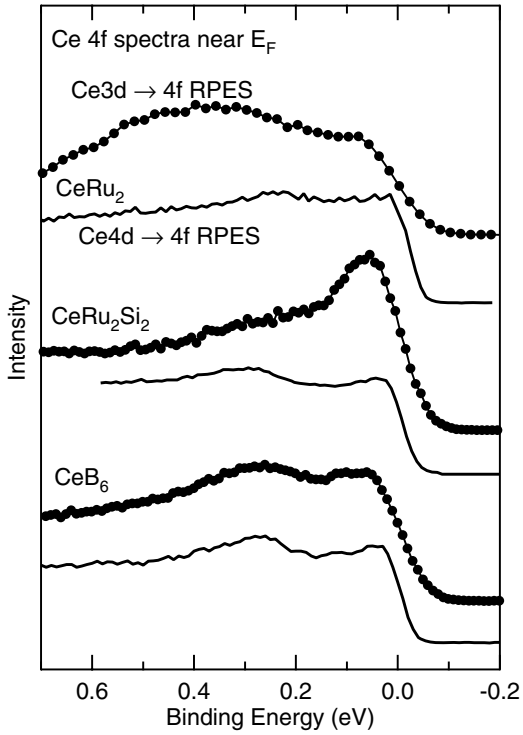

Figure 4. High-resolution bulk- and surface-sensitive Ce 4f spectra obtained by subtracting the off-resonance spectrum from the on-resonance spectrum of the Ce 3d → 4f and 4d → 4f RPES, respectively.

measurement has solved this problem by showing that the bulk Ce 4f spectrum actually do depend very much on the character of the system.

Finally, we should discuss how the bulk-sensitive Ce 4f spectra are quantitatively interpreted by models consistent with the physical properties known from other experimental methods as transport and magnetic measurements.

The dotted curves in figure 5 show the bulk-sensitive high-resolution Ce 4f spectra of $CeRu_2$, CeNi, $CeRu_2Si_2$, CeB_6 and CePdP. The 4f spectrum of CeNi, another Kondo material with T_K of about 150 K, is again characterized by a peak just below E_F and a structure around 0.2 eV but the latter is smaller than $CeRu_2Si_2$. On the other hand, the 4f spectrum of CePdP is qualitatively different from any other compounds, showing a very small intensity at E_F and a gradual increase with increasing E_B.

Transport and magnetic properties of Kondo systems at $T > T_{coh}$ have been interpreted fairly successfully by means of the single impurity Anderson model (SIAM), which consider the Ce 4f orbital as a single impurity that is hybridized with the conduction band states. Numerical studies base on applying non-crossing approximation (NCA) to SIAM (SIAM–NCA) have been able to reproduce the physical properties semi-quantitatively. Since photoemission spectra can also be calculated by means of SIAM–NCA, we have tried to reproduce, with the same set of SIAM–NCA parameters, both the photoemission spectrum and the T_K estimated from the transport and magnetic measurements. Dashed lines shown in figure 5 are the SIAM–NCA calculation results which reproduces the known bulk T_K indicated in the right-hand side of the figure. It can be seen that the Ce 4f spectra are reproduced semi-quantitatively.

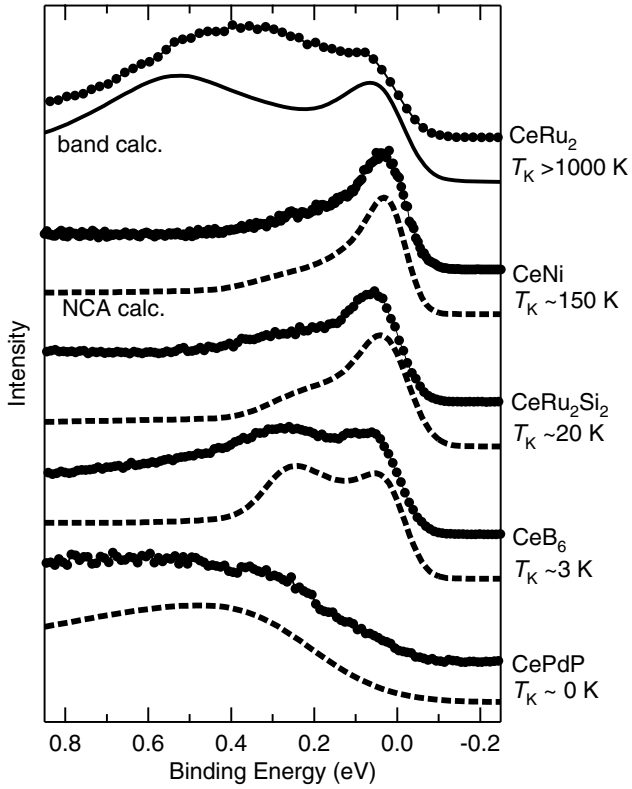

Figure 5. Comparison between the high-resolution bulk-sensitive 4f spectra and the results of the model calculation. For Ce compounds with T_K of lower than about 150 K is found to be reproduced well by the calculation based on applying the non-crossing approximation to the single impurity Anderson model. For systems with quite itinerant Ce 4f state such as $CeRu_2$, band structure calculation shows much better qualitative agreement.

Through the SIAM–NCA calculation, it is shown that the peak just below E_F found in CeNi, $CeRu_2Si_2$ and CeB_6 corresponds to the tail of a peak, called 'Kondo peak,' located at about T_K above E_F. It is also shown that the structure found near 0.2–0.3 eV corresponds to the spin–orbit satellite of the Kondo peak, which is caused by the transition of the Ce 4f electron from $J = 5/2$ to $7/2$. In the case of CePdP, the absence of both the Kondo tail and its spin–orbit satellite is found to be quite consistent with the very small T_K.

In the case of $CeRu_2$, on the other hand, SIAM–NCA calculation assuming $T_K > 1000$ K yields a spectrum similar to CeNi with a still smaller spin–orbit satellite. This strongly contradicts the experimental result. Therefore, one should conclude that SIAM is not applicable to $CeRu_2$. The Ce 4f state is so itinerant that periodic Anderson model (PAM) instead of the single impurity model is needed. To our knowledge, quantitative and realistic calculation based upon PAM is still not available. Instead, we have compared the spectrum with the Ce 4f partial density of states (PDOS) of $CeRu_2$ obtained from the band structure calculation [13]. The solid line in figure 5 shows the PDOS broadened using Lorentzian function with E_B-dependent width and Gaussian with a width corresponding to the experimental resolution. The characteristic features of the experiment, namely the broad peak and a hump near E_F, are both reproduced qualitatively. This indicates that the obtained bulk-sensitive Ce 4f spectrum is a direct evidence that the Ce 4f electrons are quite itinerant in $CeRu_2$.

2.3. Kondo resonance in the Pr 4f spectrum of heavy fermion compound $PrFe_4P_{12}$

Recently, the heavy electron mass has been found in $PrFe_4P_{12}$ under high magnetic field [14]. The crystal electric field ground state is suggested to be a non-Kramers doublet [15, 16], which is nonmagnetic but has an electric quadrupolar degree of freedom. Therefore, the heavy fermion behaviours may result from the quadrupolar Kondo effect [17, 18], which was first applied to U compounds and is in contrast to the usual spin Kondo effect in the Ce and Yb compounds.

$PrFe_4P_{12}$ is one of the Pr-based filled skutterudites PrT_4X_{12}. Among them, $PrFe_4P_{12}$ is particularly interesting due to the phase transition at around 6.5 K [19] and the Kondo-like behaviours. Recent studies suggest that the phase transition is associated with the ordering of quadrupolar moments [20, 21]. In the high-temperature phase, Kondo anomalies are found in the transport properties [14, 22]. When the low-temperature ordered phase is destroyed by high magnetic field, enormously enhanced cyclotron effective mass ($m_c^* \simeq 81m_0$), where m_0 denotes the electron mass, is observed in the de Haas–van Alphen measurement [14]. A large electronic specific heat coefficient of $C_{el}/T \sim 1.2$ J K^{-2} mol^{-1} is found under 6 T [14], which suggests the Kondo temperature T_K of the order of 10 K. These facts suggest the following scenario; quadrupolar degree of freedom of the Pr 4f state due to the non-Kramers twofold degeneracy leads to the quadrupolar Kondo effect, and the phase transition at 6.5 K resulting in the antiquadrupolar ordering is driven by the lifting of the quadrupolar degeneracy. In order for the quadrupolar Kondo effect to take place, the hybridization between the conduction band and the Pr 4f states (c–f hybridization) must be appreciably strong.

The Pr 3d $\rightarrow$ 4f XAS for $PrFe_4P_{12}$ is shown in the inset of figure 6(a). This spectrum reflects the predominant Pr^{3+} ($4f^2$) character in the initial state [10]. Spectra of $PrRu_4P_{12}$ and $PrRu_4Sb_{12}$ were also quite similar to this spectrum. On-resonance spectra were taken at 929.4 eV, around XAS maximum, and off-resonance spectra were taken at 921 eV. The on- and off-resonance spectra are compared in the main panel of figure 6(a). In the on-RPES, mainly Pr 4f contribution is enhanced. Therefore, the difference between the on- and off-RPES mainly reflects the bulk Pr 4f spectrum.

The on-RPES shown in figure 6(a) are characterized by two features. First, the on-RPES have various multiple peak structures. This feature can be interpreted by taking into account the hybridization between the valence band and the Pr 4f states (v–f hybridization) in the *final* states of PE. Second, the intensity near E_F, i.e., between E_F and $E_B \sim 0.3$ eV, is much stronger in $PrFe_4P_{12}$ than in other two systems. Such strong intensity at E_F is neither found in reported Pr 4f spectra. This feature can be attributed to the strong c–f hybridization in the *initial* state of $PrFe_4P_{12}$.

In order to get further information, we measured the Pr 3d $\rightarrow$ 4f RPES near E_F with high resolution as shown in figure 6(b). The most prominent feature is the strong peak of $PrFe_4P_{12}$ at $E_B \simeq 100$ meV. The Pr 4f spectra of $PrRu_4P_{12}$ and $PrRu_4Sb_{12}$, on the other hand, decrease continuously with some humps as approaching E_F. Spectral features similar to $PrRu_4P_{12}$ and $PrRu_4Sb_{12}$ has been found for very localized Ce systems such as CePdP shown in the last section (see figure 5), in which Ce 4f takes nearly pure $4f^1$ state. This indicates that pure $4f^2$ states are realized in $PrRu_4P_{12}$ and $PrRu_4Sb_{12}$. On the other hand, similarity in the spectrum between $PrFe_4P_{12}$ and the Kondo Ce compound such as CeB_6 suggests that the Pr $4f^2$-dominant Kondo state, with the finite contribution of $4f^1$ or $4f^3$ state, is formed in $PrFe_4P_{12}$. If this is the case, the peak at about 100 meV corresponds to the Kondo resonance (KR).

In the Kondo Ce (Yb) system, the KR is accompanied by the spin–orbit partner, the E_B of which corresponds to the spin–orbit excitation, $J = 5/2 \rightarrow 7/2$ ($J = 7/2 \rightarrow 5/2$), of the $4f^1$ ($4f^{13}$)-dominant state. A KR in Pr would then be accompanied by satellites corresponding to the excitation from the ground state ($^3H_4$) to excited states ($^3H_5$, $^3H_6$, $^3F_2$, and so on) of the

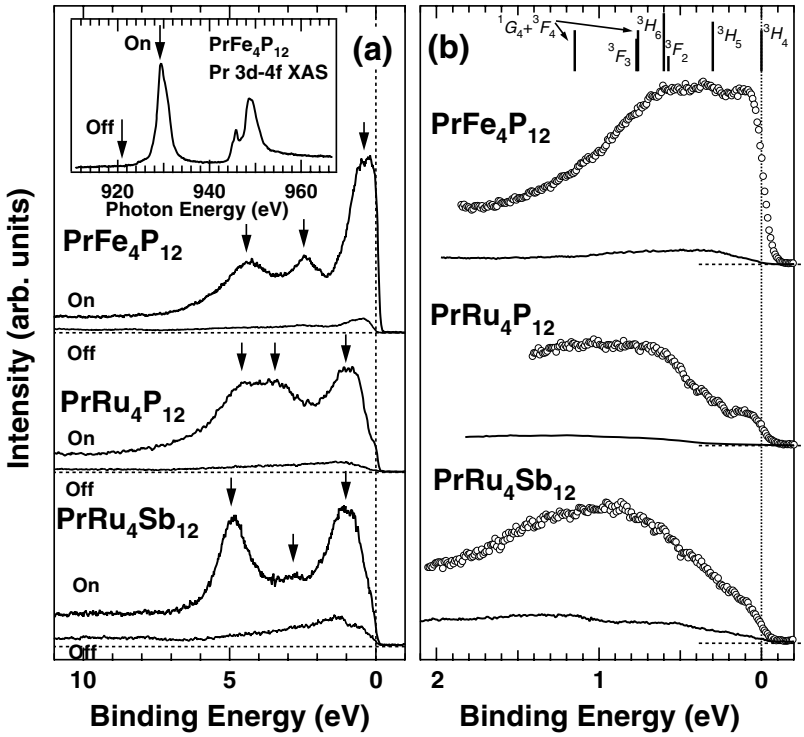

Figure 6. Pr 3d → 4f RPES of PrT_4X_{12}. (a) Off and on resonance spectra in the whole valence band region. (inset) Pr 3d → 4f XAS of $PrFe_4P_{12}$. (b) Off and on resonance spectra in vicinity of E_F.

$4f^2$ states. Figure 6 shows that the on-RPES of $PrFe_4P_{12}$ have structures at ∼0.3 and ∼0.6 eV which correspond to the lowest few excitation energies. This supports the attribution of the ∼100 meV peak to the KR.

Microscopic origin of the c–f hybridization is considered to be the P 3p–Pr 4f mixing (p–f mixing) since the nearest neighbours of the Pr atom are the twelve P atoms. The large coordination number definitely enhances the effective p–f mixing. It has been pointed out that the calculated P p PDOS of RFe_4P_{12} shows a sharp peak in the vicinity of E_F [23, 24]. This is also the case for $PrFe_4P_{12}$. Therefore, the large P 3p PDOS at E_F together with the large effective P 3p–Pr 4f mixing is interpreted to be the origin of the Kondo state in $PrFe_4P_{12}$.

3. Soft x-ray magnetic circular dichroism (XMCD) spectroscopy and microspectroscopy

Ferromagnetic materials have been attracting much attention due to their application not only to data storage and ferromagnets but also due to their potential in spin electronics and ferromagnetic shape memory. Magnetic nanostructures are especially of interest both in the storage and device points of view. In order for these applications to be successful, it is indispensable to interpret and to control the magnetic and electronic properties.

Soft x-ray magnetic circular dichroism (XMCD) is one of the powerful tools for this purpose since element-specific information about the electronic states of the magnetic electrons, such as orbital and spin contribution to the magnetic moment, can be achieved from it. Furthermore, XMCD microspectroscopy has been recently developed, which is expected to be a powerful tool to study magnetic nanostructures. In this section, we review our studies not

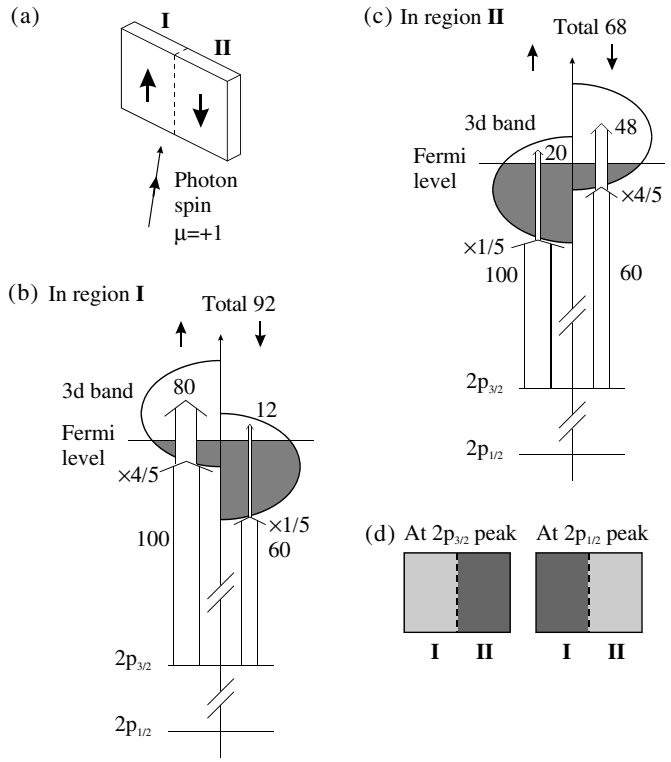

Figure 7. Principle of XMCD. (a) A model of experimental geometry. (b), (c) Probabilities of transition from $2p_{3/2}$ to 3d ferromagnetic band. (d) Resultant XMCD contrast.

only of ferromagnetic materials by means of XMCD but also of ferromagnetic microstructures by means of XMCD microspectroscopy.

3.1. Principles of XMCD and XMCD microspectroscopy

3.1.1. XMCD—origin and application. The absorption intensity of circularly polarized soft x-rays by a ferromagnetic material is different between parallel and antiparallel orientations of the magnetization direction and the photon spin [25, 26]. This phenomenon is called soft x-ray magnetic circular dichroism (XMCD). Since in the soft x-ray region, one can utilize absorption edges due to the electronic excitation from core levels to the empty states, XMCD has a powerful characteristic, namely, the element selectivity.

Strong XMCD is seen, for example, in the 2p absorption spectrum (2p XAS) of Fe. This 2p XAS is caused by the excitation of the 2p electrons of Fe to the 3d conduction band. As a model case, let us suppose as in figure 7(a) that circularly polarized soft x-rays with the photon spin of $\mu = +1$ are incident on to the sample in a negligibly small grazing angle. In this case, the magnetization direction of region I (II) is parallel (antiparallel) to the photon spin.

Consider the spin angular momentum of the Fe 3d electrons, whose direction is antiparallel to the magnetization. Since the directions of the majority spin of region I and II are downward (↓) and upward (↑), respectively, the 3d band structure of the two regions can be illustrated by figures 1(b) and (c). To simplify the following discussion, we assume that the occupancies of majority and minority spin bands are $4/5$ and $1/5$, respectively.

The 2p core level of Fe is split into two levels, namely $2p_{3/2}$ with total angular momentum $j = 3/2$ and $2p_{1/2}$ with $j = 1/2$, due to a large spin–orbit interaction. In the $j = 3/2$ (1/2) state, spin and orbital angular momenta couple parallel (antiparallel) to each other. We can take advantage of the energy difference between these levels and excite electrons from only one of the two levels into the 3d orbital.

Due to the selection rule, the circularly polarized photons with upward photon spin (see figure 7(a)) preferentially excite 2p electrons with upward orbital angular momentum into the 3d level. An additional effect of the spin–orbit interaction is that, from the $2p_{3/2}$ ($2p_{1/2}$) level, an electron with spin of the same (opposite) direction as the orbital angular momentum, namely a $\uparrow$ ($\downarrow$) electron, is likely to be excited [27]. After simple calculations and taking the transition probability of $\uparrow$ electron from the $2p_{3/2}$ to be 100, that for $\downarrow$ electron of $2p_{3/2}$ is 60, and that for $\uparrow$ ($\downarrow$) $2p_{1/2}$ electron is 20 (60).

Now, electrons excited from the 2p core level cannot move into any of the occupied sates. For example in region I, the allowed transition probability is $100 \times 4/5 = 80$ for $\uparrow$ electrons and $60 \times 1/5 = 12$ for $\downarrow$ electrons, the sum being 92 (see figure 7(b)). For region II, the allowed transition probability is in total 68 (see figure 7(c)). Since the photoabsorption intensity is proportional to the probability of the allowed transition, $2p_{3/2} \rightarrow 3d$ absorption intensity ratio between regions I and II is 92:68 in this model. For $2p_{1/2} \rightarrow 3d$, the absorption intensity ratio is 28:52. Therefore, as shown in figure 7(d), where the lighter part represents larger XAS, the $2p_{3/2} \rightarrow 3d$ ($2p_{1/2} \rightarrow 3d$) absorption is stronger in the region that is magnetized in the same (opposite) direction as the photon spin.

We define the XMCD spectrum as $I_+ - I_-$, where I_+ and I_- denote the absorption intensities with the photon spin parallel and antiparallel to the direction of the magnetic field, respectively.

Numerical analysis of the XMCD spectrum leads to quantitative information about the spin magnetic moment and the orbital magnetic moment. This is based on the sum rules proposed by Thole *et al* [28] and Carra *et al* [29].

In the case of $2p \rightarrow 3d$ XAS, the l_z sum rule can be written as

$$\langle l_z \rangle = -2 \frac{\int d\varepsilon (I_+ - I_-)}{\int d\varepsilon (I_+ + I_- + I_0)}, \tag{2}$$

where $\langle l_z \rangle$ is the average of the magnetic quantum number of the orbital angular momentum per 3d hole. I_0 is the XAS with the linearly polarized light whose polarization vector is parallel to the magnetization. The integration is taken over the whole 2p absorption region. The s_z sum rule is written as

$$\langle s_z \rangle + \frac{7}{2} \langle t_z \rangle = -\frac{3}{2} \cdot \frac{\int_{j=3/2} d\varepsilon (I_+ - I_-) - 2 \int_{j=1/2} d\varepsilon (I_+ - I_-)}{\int d\varepsilon (I_+ + I_- + I_0)}, \tag{3}$$

where t_z is the z-component of the magnetic dipole operator $\boldsymbol{t} = \boldsymbol{s} - 3\boldsymbol{r}(\boldsymbol{r} \cdot \boldsymbol{s})/|\boldsymbol{r}|^2$. The integration $\int_{j=3/2} (\int_{j=1/2})$ is taken only over the $2p_{3/2}(2p_{1/2})$ absorption region. By dividing equation (2) with equation (3), we obtain

$$\frac{\langle l_z \rangle}{\langle s_z \rangle + 7/2 \langle t_z \rangle} = \frac{4}{3} \frac{\int d\varepsilon (I_+ - I_-)}{\int_{j=3/2} d\varepsilon (I_+ - I_-) - 2 \int_{j=1/2} d\varepsilon (I_+ - I_-)}. \tag{4}$$

We should note that this equation is quite efficient. This equation stands even if the circular polarization of the light is not perfect in I_+ and I_- so long as the degree of polarization is the same for both I_+ and I_-. This equation also stands even if the magnetization of the sample is not saturated. Another advantage of this equation is that it is defined only by the difference spectrum of XMCD. It is not affected by how the background of XAS is assumed, while

equations (2) and (3) do depend on the background. If $\langle t_z \rangle$ is neglected, equation (4) yields the ratio between the spin and orbital angular momentum, which also gives $\langle l_z \rangle / \langle 2s_z + l_z \rangle$, the contribution of the orbital moment to the total magnetic moment.

3.1.2. XMCD microspectroscopy. In XMCD microspectroscopy, one magnifies and observes the microscopic distribution of XMCD on a sample. One way is to magnify the transmitted soft x-rays by using a zone-plate [30]. Another way is to magnify the emitted photoelectrons by using an electron microscope [31]. A merit of the latter, which we utilize in this paper, is that it can be applied for a sample grown on a thick substrate that soft x-rays would not penetrate. We should also note the merit of the former, namely, that observation can be carried out even in applied magnetic fields since it is a photon-in, photon-out measurement.

The electron microscope that is used in XMCD microspectroscopy is called a photoelectron emission microscope (PEEM). In a PEEM, electrons emitted from the sample are projected on a fluorescent screen by electron lenses. When used in XMCD microspectroscopy, the PEEM is set to observe the secondary electrons emitted as a consequence of the absorption of soft x-rays. It is known that the intensity of the secondary electrons depends approximately linearly upon the photoabsorption intensity. Therefore, by observing a PEEM image, the distribution of the XAS intensity can be observed.

3.2. XMCD study of the orbital magnetic moment in transition metal-based ferromagnets

The orbital magnetic moment or the contribution of the orbital angular momentum to the magnetic moment has been known to be not negligible even in metallic 3d transition metal systems. The orbital magnetic moment plays a relevant role in magnetic anisotropy and magneto-optical effects, both of which are important also from an applied point of view. In order to understand the mechanism that determines the size of the orbital magnetic moment, a study of compounds with different compositions or different chemical environments is very useful. For this purpose, we chose intercalates Fe_xTiS_2 in spin glass and ferromagnetic phases [32] and ferromagnetic Heusler alloys containing Co [33].

XMCD was measured in the Faraday configuration at BL25SU of SPring-8 [9]. The resolution was set to about 80 meV around $h\nu$ 800 eV. XAS spectrum was measured by the total electron yield (TY) method in which the sample current was directly measured while scanning $h\nu$. The XMCD spectrum was taken by reversing the direction of the magnetic field H (1.4 T) applied to the sample at each $h\nu$ while the helicity of the light was fixed.

3.2.1. Magnetic states of Fe and Ti in the intercalates Fe_xTiS_2. It has been revealed that Fe intercalates Fe_xTiS_2 have itinerant electron magnetism associated with the intercalated Fe 3d electrons and show various interesting magnetic behaviours [35, 36]. The ground state of Fe_xTiS_2 is either spin glass, cluster glass or ferromagnetic depending on the guest Fe concentration x.

Figure 8 shows the Fe 2p XAS spectra I_+ and I_- of Fe_xTiS_2 at 30 K (under the order temperatures of these samples) for three different Fe concentrations, $x = 1/3$, $1/4$, and 0.10. The XAS spectra are normalized to the Fe concentration. They consist of the $2p_{3/2}$ and $2p_{1/2}$ components split by the core hole spin–orbit interaction. The bottom curves show difference spectra $I_+ - I_-$, i.e., XMCD spectra. The XMCD spectra are characterized by typical positive and negative peaks in the $2p_{3/2}$ and $2p_{1/2}$ components with a positive peak in the threshold region of the $2p_{3/2}$ XAS for all three concentrations. The $2p_{3/2}$ edge shows a weak negative and positive dichroism at 3.5 eV and 7.5 eV above the main peak, respectively. The line shapes of XMCD spectra for $x = 1/4$ and 0.10 are almost identical. The $2p_{3/2}$ and $2p_{1/2}$ XMCD peak

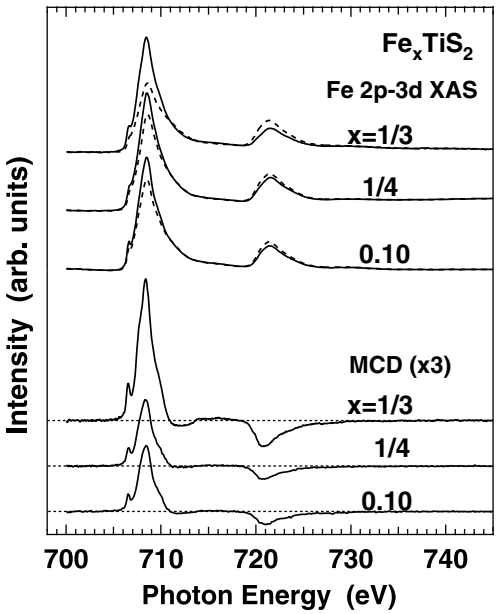

Figure 8. Fe 2p $\rightarrow$ 3d XMCD of Fe_xTiS_2. In the top panel, solid (dashed) lines show I_+ (I_-).

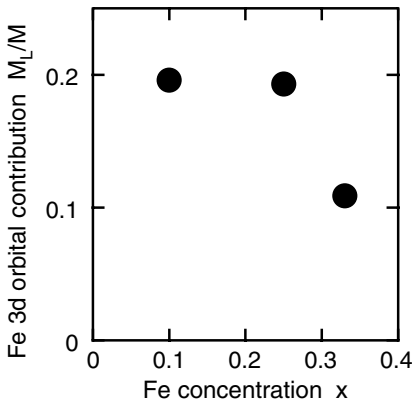

Figure 9. Ratio of the orbital contribution to the Fe 3d magnetic moment of Fe_xTiS_2.

intensities for $x = 1/3$ are about twice as large as those for other concentrations. This indicates that the magnetic moments contributing to the XMCD decrease for decreasing x. The origin of the decrease might be that magnetic moments of $x = 1/4$ and 0.10 are not saturated because magnetic coercive forces are higher than the applied magnetic field 1.4 T, the maximum field that can be applied to the sample in our equipment.

By means of the sum rules equations (2) and (3), the contribution of the orbital magnetic moment to the total magnetic moment $\langle l_z \rangle / \langle 2s_z + l_z \rangle$ of the Fe 3d electrons is estimated. Figure 9 shows its x-dependence. Apparently, the orbital contribution changes its value qualitatively between $x = 1/4$ and $1/3$. This boundary is near to that between spin glass and ferromagnetic phases. Therefore, it is suggested that orbital contribution and spin glass to ferromagnetic transition are governed by the same mechanism. It is possible that they

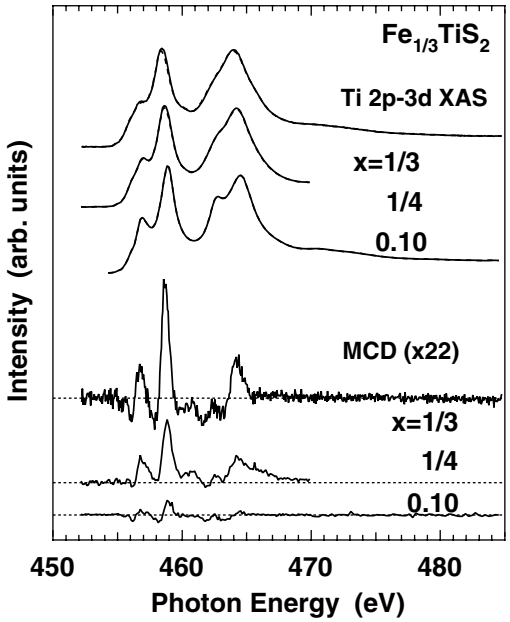

Figure 10. Ti 2p → 3d XMCD of Fe_xTiS_2.

are both governed by the degree of itinerancy of the Fe 3d electrons, which definitely should depend upon the Fe concentration x. It has been discussed that when the degree of itinerancy increases in ordered alloys, the orbital contribution decreases [37]. It is quite probable that the ferromagnetism of this system is characterized by itinerant ferromagnetism and that when x is small enough the ferromagnetic interaction is not large enough leading to the spin glass state.

The Ti 2p XMCD spectra at 30 K for $x = 1/3$, $1/4$, and 0.10 are shown in figure 10. For $x = 1/3$, the line shape of Ti 2p XAS spectra resembles that of the V 2p XAS spectra in $CaVO_3$ which has the d^1 configuration in the initial ground state. It suggests that in $Fe_{1/3}TiS_2$ the d^1 configuration is dominant due to the charge transfer from the Fe atom to the Ti atom. The $2p_{3/2}$ and $2p_{1/2}$ edges show shoulders at around 1.5 eV below the main peaks, reflecting the t_{2g}–e_g crystal field splitting. These multiplet structures become more prominent with the decrease of the Fe concentrations x. It is known in the host material 1T-TiS_2 that the multiplet structure is clearer [38]. The origin of the spectral change as x decreases is interpreted to be that the character of the final states changes from the $2p^53d^2$ and $2p^53d^3\underline{L}$ to the $2p^53d^1$ and $2p^53d^2\underline{L}$ configuration. In other words, the initial state changes from an d^1-like to a d^0-like state. The Ti 2p XAS shows clear XMCD as shown in the bottom of figure 10, suggesting that a magnetic moment is induced on the Ti atom due to the charge transfer of the Fe 3d electrons, i.e., through the hybridization with the Fe t_{2g} orbitals. The magnitude of the XMCD spectra decreases with x, suggesting the number of Ti atoms whose orbitals are hybridized with Fe orbitals decrease with lower Fe atom concentrations.

3.2.2. Orbital contribution of the Co 3d in Co_2YSn. Heusler alloys belong to a group of ternary intermetallic compounds with the stoichiometric composition of X_2YZ ordered in an $L2_1$ type structure, many of which with transition metal X and Y atoms exhibit magnetic order [39]. The third element Z is a nonmagnetic metal or nonmetallic element. The Co atoms mainly carry the magnetic moment in the Co-based Heusler alloys Co_2YZ except for

Co_2MnSn. The Co_2YZ are of particular interest because the magnetic moment per Co atom is known to have values ranging from 0.3 to 1.0 μ_B in these alloys [40]. Co_2TiSn, Co_2ZrSn, and Co_2NbSn exhibit ferromagnetism below Curie temperatures T_C at around 371, 448, and 105 K, respectively [41]. Among them Co_2NbSn is of special interest since it undergoes a structural phase transition from the cubic $L2_1$ to orthorhombic phase at 253 K [42].

According to a band calculation of Co_2MnSn, Co_2TiSn, and Co_2TiAl, there is a peak near the Fermi level (E_F) in the partial density of states (PDOS) of the Co d bands as a characteristic feature of Co_2YZ [43]. The PDOS of the Co d states, especially the energy position of this peak with respect to E_F, depends very much on the elements in the Y and Z sites. This situation is expected to explain the above mentioned composition dependence of the magnetic moments. The change in the band structure should also lead to the change in the contribution of the orbital magnetic moment to the total magnetic moment of Co.

In order to investigate how the orbital angular momentum on the Co atom in Co_2YSn varies and also to clarify the responsible mechanisms, we have carried out measurements of XMCD of the Co 2p $\rightarrow$ 3d excitation for Co_2YSn (Y = Ti, Zr, and Nb).

In figure 11 are shown the Co 2p $\rightarrow$ 3d XAS spectra I_+ and I_- and their difference spectra $I_+ - I_-$, i.e., the XMCD spectra at 100 K for Y = Ti and Zr and at 50 K for Y = Nb. The XAS spectra of these three alloys consist of the $2p_{3/2}$ and $2p_{1/2}$ components split by the core hole spin–orbit interaction. In the $2p_{3/2}$ component region, the spectral line shapes are noticeably different for three alloys as seen in the insets of figure 11 between 777 and 782 eV. The multiplet structure is not recognized in conventional XAS spectra in Heusler alloy systems [44], because the multiplet splitting of intermetallic compounds is generally small compared with ionic compounds. However, clear multiplet structures are seen in these spectra owing to the high energy resolution ($\sim$80 meV). Three characteristic peaks are recognized at around 778.5, 779.1 and 780.0 eV for all three alloys. Although these peaks are located at quite similar photon energies, peak intensities are different from each other. In Co_2ZrSn, the 778.5 eV peak is much stronger than the other two peaks. Both 779.1 and 780.0 eV peaks become stronger in Co_2TiSn and Co_2NbSn, or the 778.5 eV peak is relatively suppressed. The origin of these multiplet peaks is due to the interplay of two effects, namely, the exchange and Coulomb interactions between the core hole and unpaired electrons in the valence bands, and hybridization between the 3d and surrounding electronic states.

XMCD spectra of Co_2YSn (Y = Ti, Zr, and Nb) are shown in the bottom of figure 11. For all three alloys the positive and negative peaks can be seen in the $2p_{3/2}$ and $2p_{1/2}$ regions, respectively. That means the spin magnetic moment of the Co atom in these alloys is oriented in the same direction as the net magnetization, because the 3d states with the negative spin are more occupied than those with the positive spin [37]. The XMCD intensity in the $2p_{3/2}$ region is much larger and sharper than that in the $2p_{1/2}$ region as in other Co intermetallic compounds [37]. In addition, the long tail can be seen on the higher-photon-energy side of the $2p_{1/2}$ XAS. The magnitude of the XMCD spectrum in the whole photon energy region is smaller for Co_2NbSn than for Co_2TiSn and Co_2ZrSn. The smaller XMCD may be originating from the situation that the applied magnetic field is not enough to saturate the magnetization of the sample [45]. Although the $2p_{3/2}$ main XMCD peak of these three alloys is located at quite similar photon energy of 778.5 eV, the line shapes and peak intensities are obviously different from each other. For example, Co_2TiSn, Co_2ZrSn, and Co_2NbSn have their additional characteristic peak at 1.2, 2.0 and 0.6 eV higher energies of the $2p_{3/2}$ main peak, respectively. In particular, the $2p_{3/2}$ main XMCD peak is broader in Co_2NbSn than in Co_2TiSn and Co_2ZrSn. The broadness of the Co_2NbSns XMCD peak may be a consequence of the smallness of the 778.5 eV peak in XAS, which can be attributed to the more occupied minority spin band as described below.

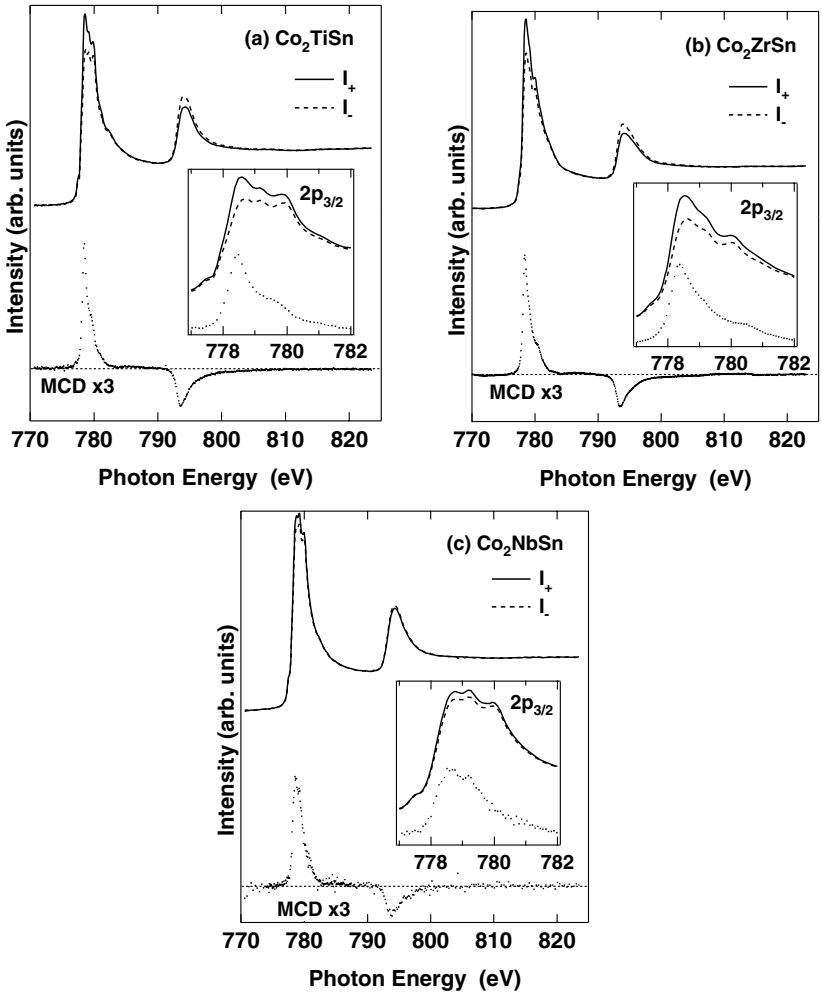

Figure 11. Co 2p → 3d XMCD of Co_2YSn (Y = Ti, Zr, Nb).

The orbital contribution to the magnetic moment of the Co 3d electrons $\langle l_z\rangle/\langle 2s_z + l_z\rangle$ is estimated by means of the sum rule as 0.09, 0.15 and 0.19 for Co_2TiSn, Co_2ZrSn and Co_2NbSn, respectively.

The main features in the band structures of Co_2TiSn and Co_2ZrSn are quite similar to each other with respect to the energy positions and the PDOS. On the other hand, the band structure of Co_2NbSn is quite different. Namely, the minority spin band of Co_2NbSn is shifted to lower energy and is more occupied than in Co_2TiSn and Co_2ZrSn. If the contribution of the orbital magnetic moment is mostly determined by the overall band structures, we expect that the orbital contributions of Co_2TiSn and Co_2ZrSn are comparable to each other, and that of Co_2NbSn is quite different from these two. However, the experimental result shows that $\langle l_z\rangle/\langle 2s_z + l_z\rangle$ of these compounds are all quite different from each other. Therefore, the orbital contribution must be influenced also by factors other than the overall band structures.

It is believed in transition metal compounds that the orbital contribution becomes larger when the 3d states are more localized. Therefore, the difference in $\langle l_z\rangle/\langle 2s_z + l_z\rangle$ between

Co_2TiSn and Co_2ZrSn, whose band structures resemble each other, suggests that the Co 3d electronic state is more localized in Co_2ZrSn than in Co_2TiSn. When we discuss the difference in the degree of localization between Co_2TiSn and Co_2ZrSn, at least two aspects should be considered. The first is the effect of the character of the d electrons at the Y site. Namely, Zr 4d electrons are more itinerant than Ti 3d electrons, which would make the electronic band of Co_2ZrSn more itinerant than Co_2TiSn. On the other hand, the second factor is the direct hybridization between the Co 3d electronic states of the neighbouring Co sites. While the nearest neighbour of Co is Y and Sn sites, the next nearest neighbour is Co itself. Since the Co–Co distance is only 1.15 times larger than Co–Y and Co–Sn distance, direct hybridization between the Co 3d states is not negligible at all. Since the lattice constant of Co_2ZrSn ($a = 6.245$ Å) is larger than Co_2TiSn ($a = 6.077$ Å), the Co 3d's direct hybridization is smaller in Co_2ZrSn than in Co_2TiSn. This would make the Co 3d states of Co_2ZrSn more localized than Co_2TiSn. The degree of Co 3d localization is hence influenced by two competing effects. It should be quite difficult to estimate theoretically which effect is stronger. However, the present experimental result indicates that the effect of the direct hybridization between the neighbouring Co 3d states is stronger in the present Co Heusler alloys.

When Co_2ZrSn and Co_2NbSn are compared, on the other hand, the drastic change in the band structures mentioned above can be the main reason for the different $\langle l_z\rangle/\langle 2s_z + l_z\rangle$. According to a discussion based on the second order perturbation theory, the orbital magnetic moment of a cubic 3d compound arises from the mixing either in the t_{2g} orbitals or between t_{2g} and e_g orbitals. Therefore, a difference in the contribution of e_g and t_{2g} states in the Co 3d band at E_F would lead to a difference in $\langle l_z\rangle/\langle 2s_z + l_z\rangle$.

3.3. XMCD microspectroscopy of transition metal magnetic microstructures

Magnetic domain structures of microstructured polycrystalline Co films [46, 47] and spin reorientation transition in epitaxial Co/Ni bilayer [48] were studied by means of XMCD microspectroscopy.

The measurements were performed at the twin helical undulator beamline for soft x-ray spectroscopy BL25SU of SPring-8 in Japan [9]. The photon spin was chosen by closing one undulator and fully opening the other. The light was incident on to the sample at a grazing angle of 30° from the surface. The set-up of the photoemission microscope (Focus IS-PEEM) was as previously described [34]. By setting the contrast aperture to 70 μm and the extractor voltage to 10 kV, a field of view of about 50–100 μm and a lateral resolution of about 0.4 μm were achieved.

3.3.1. Magnetic domains and magnetization process. Microstructures of 30 nm thick polycrystalline Co film were made on a Si substrate by electron-beam lithography and the lift-off technique. Both the length and the width of the rectangles were changed from 0.5 to 32 μm, in steps of a factor of 2.

In order to improve the magnetic contrast, we took PEEM images at two photon energies corresponding to Co $2p_{3/2}$ and $2p_{1/2} \rightarrow$ 3d transitions under the same photon spin and generated an image of asymmetry, $(I(2p_{3/2}) - I(2p_{1/2}))/(I(2p_{3/2}) + I(2p_{1/2}))$, which depends linearly on the projection of the magnetic moment on the photon spin. Pulsed magnetic field for magnetization was applied to the in-plane direction, i.e., parallel to the surface, by discharging a capacitor through a coreless solenoidal coil, and measurement was carried out under zero field.

Figure 12 shows the asymmetry image of PEEM-XMCD for the as-made rectangular microstructures. The circularly polarized soft x-ray was incident in the direction shown by

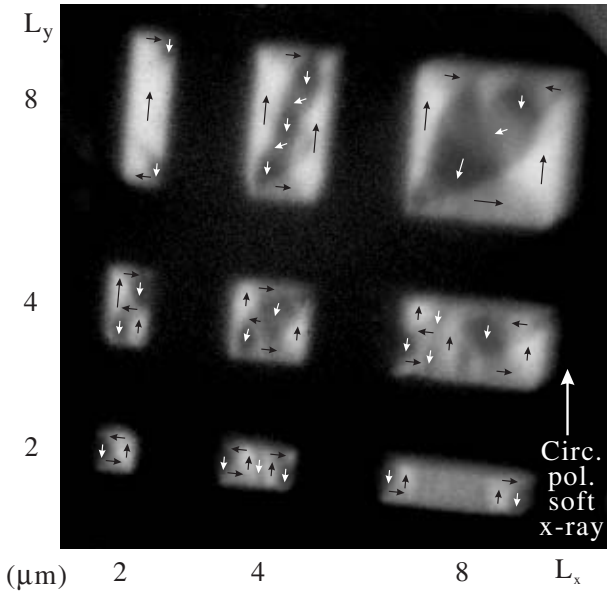

Figure 12. Magnetic domain structures obtained by the PEEM-XMCD of the as made magnetic microstructures made of 30 nm thick polycrystalline Co film.

the arrow on the lower right-hand corner with a grazing angle of 30° from the sample surface. White and dark grey parts correspond to the domains magnetized upward and downward, as indicated by arrows. Light grey parts are magnetized to nearly horizontal directions, and whether they are right or left can be deduced from the geometrical connection of the domains. In each microstructure is realized such a domain structure that the stray field is decreased. Nearly 90° domain walls are most commonly seen and some nearly 180° domain walls can also be seen.

Next, we investigated the magnetization reversal processes of $L_x < L_y$ rectangles. For this, we chose $L_x < L_y$ rectangles that were saturated by the largest available 288 Oe downward pulse, and investigated the effect of upward pulses. Figure 13(a) shows, as an example, the magnetization reversal processes for $L_x \times L_y = 2 \times 8$ and 4×8 μm^2 by magnetic field pulses. The domain structure of the 2×8 μm^2 rectangle was not changed by magnetic field pulses of 36–90 Oe and was flipped from the downward remanence to the upward remanence by the magnetic field pulse of 108 Oe. On the other hand, the 4×8 μm^2 rectangle was not changed by the 36 Oe pulse, was changed from the downward remanence to a vortex type structure by the 54 Oe pulse and was changed to the upward remanence by the 108 Oe pulse. We define two transition fields for each rectangle. The coercive field H_C is the strength of the magnetic field pulse by which the downward saturated structure is changed into a different structure. The saturation field H_S is the strength of the magnetic field pulse by which the rectangle is saturated in the upward direction. Then, $H_C = H_S = 108$ Oe for the 2×8 μm^2 rectangle and $H_C = 54$ Oe and $H_S = 108$ Oe for the 4×8 μm^2 rectangle.

The L_x and L_y dependences of H_C and H_S are shown in figure 13(b). Rectangles can be categorized into two groups. The saturated domain structure of one group is directly transformed into the reversed saturation, which leads to $H_C = H_S$. This type corresponds to what Hefferman *et al* [49] called 'type A' and is seen in the smaller L_x region of figure 13(b). In the other group, named 'type B,' the saturated domain structure is first transformed into the

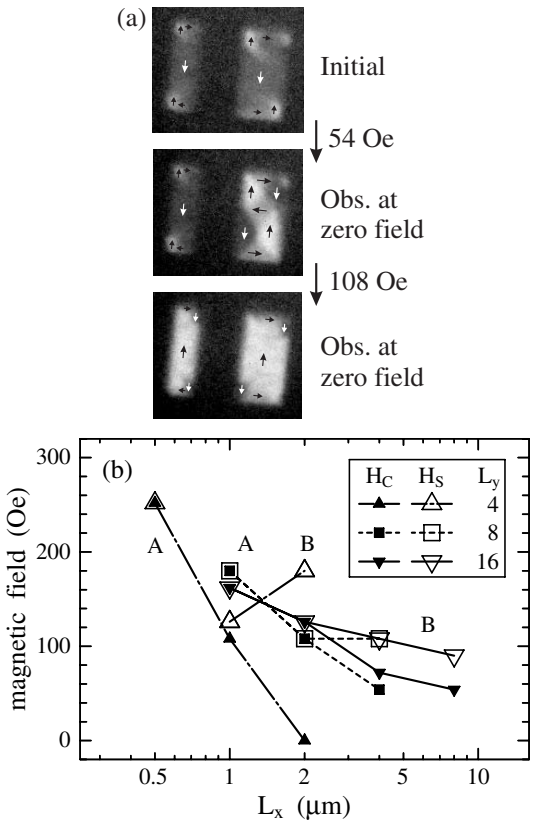

Figure 13. (a) Magnetization reversal of 2 × 8 (left) and 4 × 8 μm^2 (right) rectangles. (b) Dependence of the coercive field H_c and the saturation field H_s on the width L_x and the length L_y of the Co rectangles.

vortex structure at H_C, and then is saturated in the direction of the pulse at H_S. This type is recognized in the larger L_x region of figure 13(b). It might seem unnatural that the H_C of 2 × 4 μm^2 is zero. This reflects the experimental result that after this rectangle was saturated by the downward pulse, it transformed by itself into a vortex structure. This indicates that the vortex structure is very stable in this rectangle. The trigger for the transformation might be thermal fluctuation or an external stray field.

Figure 13(b) shows that for a fixed L_y, H_C decreases monotonically as L_x increases. The magnitude of the slope seems to be larger for smaller L_y. What might be happening at H_C in the magnetization process is that the end domains such as the white areas in the 'initial' image of $L_x \times L_y = 4 \times 8$ μm^2 in figure 13(a) grow until the tips of the domains touch each other [49]. If we compare such end domains of rectangles between different L_x as $L_x \times L_y = 4 \times 8$ and 2 × 8 μm^2, the end domains of the rectangle with larger L_x extend more into the rectangle. Therefore, the switching process is realized by a smaller field pulse in a rectangle with a larger L_x.

On the other hand, the slope of H_S in the type B region might be due to the shape anisotropy. However, the shape anisotropy of a thin film should be weak. In fact, the H_S values in the type B region are all about 100 Oe, except for $L_x \times L_y = 2 \times 4$ μm^2. This H_S value of about 100 Oe can be considered as the saturation field of an infinite plane of 30 nm

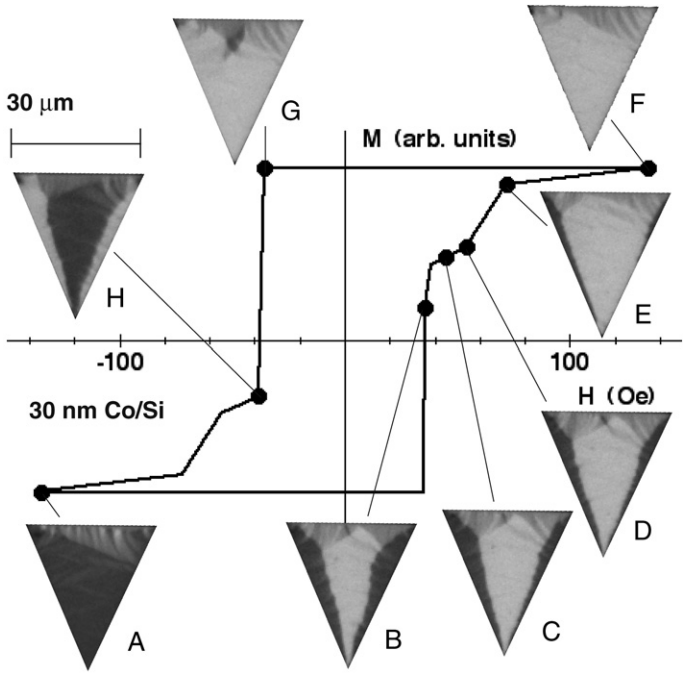

Figure 14. Transformation of the magnetic domain structure of the triangular Co microstructure by magnetic field pulses, corresponding to a major hysteresis loop.

thick Co film. The exceptionally large value of H_S for 2×4 μm^2 can be attributed to the above mentioned strong stability of the vortex domain structure in it. The stability of such structures becomes irrelevant for larger rectangles.

The transformation processes of the magnetic domains of a triangular microstructure caused by two sequential series of magnetic field pulses are summarized in figures 14 and 15. In these figures, circularly polarized light of photon spin $\mu = +1$ was incident on to the sample from the bottom to the top in the figure. Therefore, the lightest part of the image, corresponding to the largest asymmetry A, is magnetized in the upward direction and the darkest part is magnetized in the downward direction. The regions with the medium contrast, found mainly near the top edge of the triangle, are magnetized to the right or left direction. The region near an edge of the triangle is magnetized along a direction parallel to the edge. The total magnetization projected on to the direction of the photon spin in each state was estimated by integrating the asymmetry A over the whole triangle. The direction of the pulsed magnetic field was nearly parallel to the photon spin, namely, positive magnetic field $H > 0$ corresponds to an upward magnetic field.

In figure 14 is shown the transformation corresponding to the major hysteresis loop. Namely, the direction of the magnetic field is reversed after saturation is achieved. However, we should note that the 'hysteresis loop' drawn here is not a hysteresis loop in the normal sense since the images are those under zero field after applying the magnetic field pulse. Starting from a saturated domain structure as in images (A) and (F), magnetic field pulses of the opposite direction with increasing magnitude were applied. The magnetization reversal process is revealed to start with the nucleation of a small magnetic domain near the top edge, as seen in image (G). Next, this domain grows downward until it touches the bottom apex as

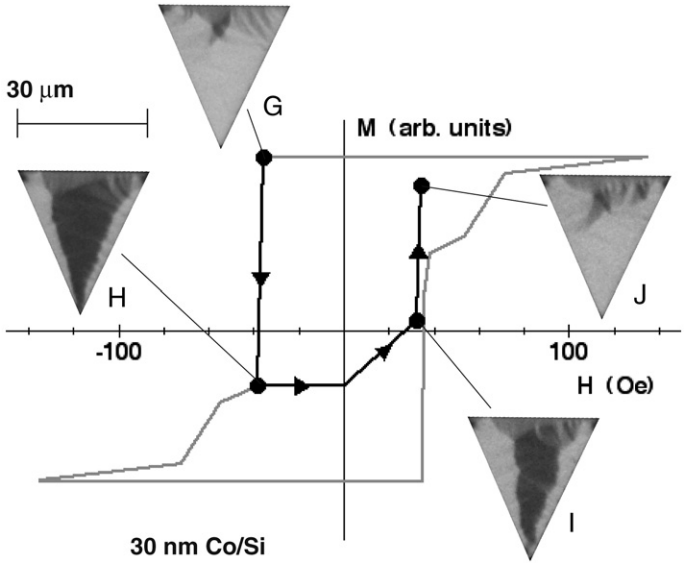

Figure 15. The same as in figure 14 but for a minor hysteresis loop.

in images (H) and (B). By increasing the magnitude of the magnetic field pulses, the magnetic domain in the centre gradually expands to both sides, as seen in images (C), (D) and (E). By applying a sufficiently large magnetic field, the domains with the other magnetization direction in both sides are wiped out, leaving some region not saturated near the top edge, as in images (A) and (F).

Figure 15 shows the transformation of the domain structure corresponding to a minor hysteresis loop. After a downward magnetized domain was made in the central part as in the image (H) by downward magnetic field pulses, upward pulses were applied. Then, as shown in the image (I) and (J), the area of the upward magnetized domain in the both sides increased, instead of a new upward magnetized domain being generated near the top edge. The contrast is totally opposite between, for example, images (I) and (B) although they are at about the same position in the H–M space. This topological contrast is interpreted to be connected to the difference between the major and minor hysteresis loops.

3.3.2. Spin reorientation transition in an epitaxial Co/Ni bilayer. The study of magnetization easy directions is quite important in the field of magnetic thin films and superstructures. At room temperature, by increasing the thickness of the epitaxially grown Ni film on Cu(001), the magnetization easy axis changes from in plane to out of plane at around 10 monolayers (ML) and then again to in plane at around 60–70 ML. Furthermore, evaporation of a few monolayers of Co on top of the Ni film in the out-of-plane thickness region makes the easy axis in plane [50, 51].

In order to study the mechanism of this spin reorientation transition, a crossed double-wedged Co/Ni/Cu(001) was prepared. Namely, Ni was evaporated on Cu(001) in a wedge shape with the thickness varying in the x direction in the range of 0–14 ML, on top of which 0–4 ML Co was evaporated whose thickness was varied in the y direction. The sample was not intentionally magnetized either during or after the sample preparation.

In order to use the XMCD sum rules, equations (2) and (3), PEEM images were taken for each photon spin at 105 photon energy points between 845 and 890 eV which covers the Ni

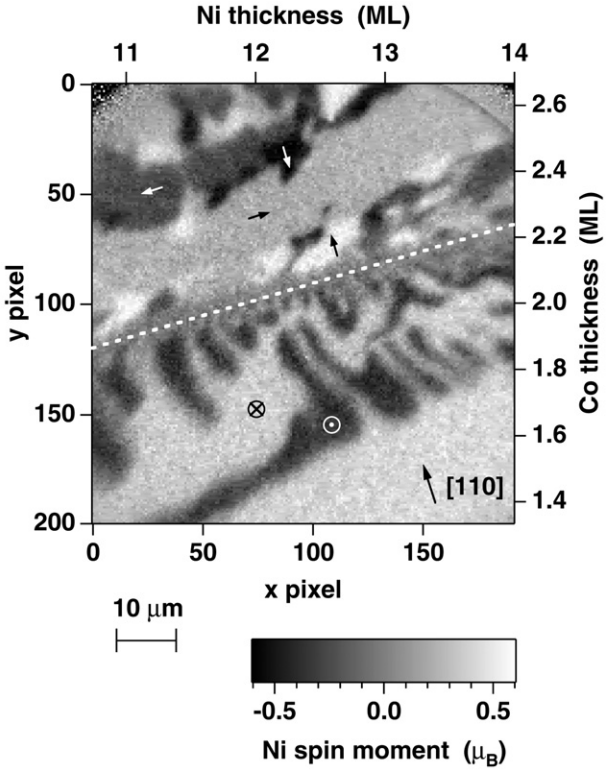

Figure 16. Distribution of the Ni spin magnetic moment for Co/Ni/Cu(001) double wedge.

$2p_{3/2}$ and $2p_{1/2}$ photoabsorption regions. Since each image consisted of $192 \times 200 = 38\,400$ pixels, this yields 38 400 sets of I_+ and I_- spectra.

Figure 16 shows the distribution of M_S, whose quantization axis is the incident direction of the soft x-ray, pointing to the y-axis of the figure with an angle of 30° from the sample surface. The whole area can be divided into two by the dotted white line, above which are four levels of contrast and below which are only two levels. When Ni is magnetized in the plane, the magnetization easy directions are the four directions equivalent to [110] shown in the lower right-hand corner of the figure. Therefore, the four levels of contrast in the upper part correspond to the four directions of magnetization shown by the arrows. On the other hand, the two levels in the lower part correspond to the two out-of-plane directions, one going into the sheet (⊗) and the other coming out of the sheet (⊙).

It is hence apparent that magnetization easy direction is changed from out of plane to in plane as functions of thicknesses of both Co and Ni films. The white dotted line corresponding to the spin reorientation transition line was approximately $d_{Co} = 0.116\,d_{Ni} + 0.62$, where d_{Co} and d_{Ni} are the thicknesses of Co and Ni in units of ML. Approaching the spin reorientation transition from the perpendicularly magnetized area in the bottom, the average domain size seems to be decreasing. Although it is hard to tell from the present image, the interior of the spin reorientation transition region probably consists of small unresolved domains.

By combining figure 16 and the distribution of M_L shown in figure 17, it was found that the orbital magnetic moment changes its value between in-plane (0.034 μ_B) and out-of-plane (0.052 μ_B) magnetized phases, while the spin magnetic moment was about the same value of

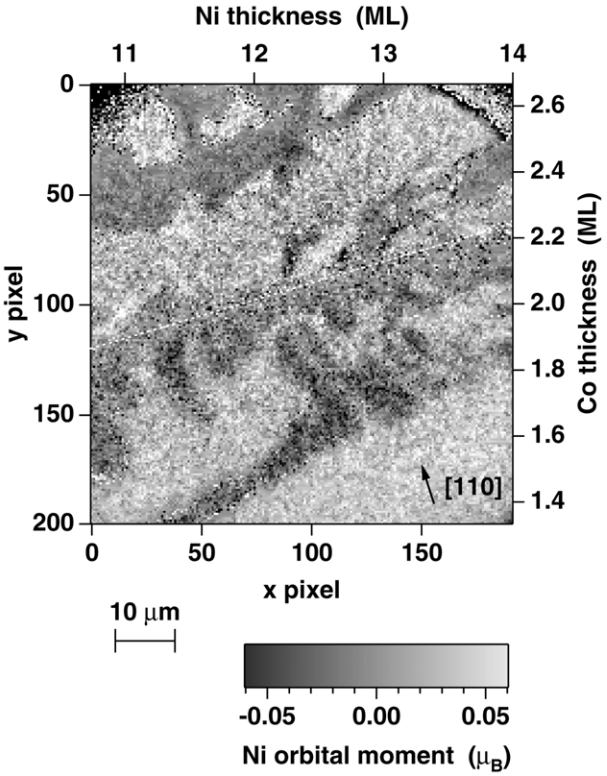

Figure 17. Distribution of the Ni orbital magnetic moment for Co/Ni/Cu(001) double wedge.

0.65 μ_B for both phases. This indicates that the gain of the energy caused by the spin–orbit interaction is larger in the out-of-plane phase than in the in-plane phase, which is consistent with the fact that the magnetization easy direction of the Ni film alone is out of plane in this thickness range. The energy difference between in-plane and out-of-plane magnetizations, in other words the magnetic anisotropy energy, was estimated to be 50–90 μeV/Ni atom.

4. Future perspectives

The success of the high-resolution bulk-sensitive photoemission has initiated development of angle-resolved photoemission in the soft x-ray region. Although the resolution in the reciprocal lattice vector becomes worse than in the case of $h\nu = 20$–100 eV measurements, it is still as good as about a tenth of the size of the Brillouin zone. Therefore, fermiology of the bulk can be investigated, which is definitely needed for all the samples that had been studied by means of the surface-sensitive angle-resolved photoemission.

Still higher bulk sensitivity should also be sought. For this purpose, photoemission with incident photons with $h\nu$ of the order of 10 keV is now attracting much attention. If the development of both light source and electron energy analyser is successful, energy resolution of 30 meV might be possible at $h\nu \sim 10$ keV.

It is expected that XMCD continues to be an indispensable tool for designing and developing functional ferromagnetic materials. Its element selectivity is especially important since it is becoming more and more important to optimize the composition of multinary compounds, for example in the development half metals and magnetic semiconductors.

Needless to say, XMCD microspectroscopy is one of the most promising tools in promoting magnetic nanoscience and nanotechnology. Drastic improvement of the spatial resolution is expected to be realized in the near future by the development of PEEM with resolution of 2 nm [52].

Dynamics of the magnetic domain structures has also become attainable by synchronizing magnetic field pulses and synchrotron radiation pulses [53]. Development of the hard disk with recording density of 1 Tbit/in^2, for example, will be drastically accelerated if the magnetic domain dynamics can be observed with a special resolution of a few nanometres and a time resolution of a few tens of nanoseconds.

References

[1] Sekiyama A, Iwasaki T, Matsuda K, Saitoh Y, Ōnuki Y and Suga S 2000 *Nature* **403** 396
[2] Sekiyama A *et al* 2000 *J. Phys. Soc. Japan* **69** 2771
[3] Iwasaki T *et al* 2002 *Phys. Rev.* B **65** 195109
[4] Sekiyama A *et al* 2002 *Solid State Commun.* **121** 561–4
[5] Yamasaki A, Imada S, Nanba T, Sekiyama A, Sugawara H, Sato H, Sekine C, Shirotani I, Harima H and Suga S 2004 *Phys. Rev.* B **70** 113103
[6] Fuggle J C 1990 *Proc. Int. School of Physics 'Enrico Fermi'* vol 108 (Elsevier: Amsterdam) p 127
[7] Weschke E, Laubschat C, Simmons T, Domke M, Strebel O and Kaindl G 1991 *Phys. Rev.* B **44** 8304
[8] Duò L, De Rossi S, Vavassori P, Ciccacci F, Olcese G L, Chiaia G and Lindau I 1996 *Phys. Rev.* B **54** 17363
[9] Saitoh Y *et al* 1998 *J. Synchrotron Radiat.* **5** 542
[10] Thole B T, van der Laan G, Fuggle J C, Sawatzky G A, Karnatak R C and Esteva J-M 1985 *Phys. Rev.* B **32** 5107
[11] Jo T and Kotani A 1988 *Phys. Rev.* B **38** 830
[12] Sekiyama A, Suga S, Iwasaki T, Ueda S, Imada S, Saitoh Y, Yoshino T, Adroja D T and Takabatake T 2001 *J. Electron. Spectrosc. Relat. Phenom.* **114–116** 699
[13] Tanaka S, Harima H and Yanase A 1998 *J. Phys. Soc. Japan* **67** 1342
[14] Sugawara H, Matsuda T D, Abe K, Aoki Y, Sato H, Nojiri S, Inada Y, Settai R and Ōnuki Y 2002 *Phys. Rev.* B **66** 134411
[15] Nakanishi Y, Simizu T, Yoshizawa M, Matsuda T D, Sugawara H and Sato H 2001 *Phys. Rev.* B **63** 184429
[16] Aoki Y, Namiki T, Matsuda T D, Abe K, Sugawara H and Sato H 2002 *Phys. Rev.* B **65** 064446
[17] Cox D L 1987 *Phys. Rev. Lett.* **59** 1240
[18] Andrei N and Destri C 1984 *Phys. Rev. Lett.* **52** 364
[19] Torikachvili M S, Chen J W, Dalichaouch Y, Guertin R P, McElfresh M W, Rossel C, Maple M B and Meisner G P 1987 *Phys. Rev.* B **36** 8660
[20] Keller L, Fischer P, Herrmannsdorfer T, Donni A, Sugawara H, Matsuda T, Abe K, Aoki Y and Sato H 2001 *J. Alloys Compounds* **323/324** 516
[21] Iwasa K, Watanabe Y, Kuwahara K, Kohgi M, Sugawara H, Matsuda T D, Aoki Y and Sato H 2002 *Physica* B **312/313** 834
[22] Sato H, Abe Y, Okada H, Matsuda T D, Abe K, Sugawara S and Aoki Y 2000 *Phys. Rev.* B **62** 15125
[23] Harima H and Takegahara K 2002 *Physica* B **312/313** 843
[24] Sugawara H, Abe Y, Aoki Y, Sato H, Hedo M, Settai R, Ōnuki Y and Harima H 2000 *J. Phys. Soc. Japan* **69** 2938
[25] Schütz G, Wagner W, Wilhelm W, Kienle P, Zeller R, Frahm R and Materlik G 1987 *Phys. Rev. Lett.* **58** 737
[26] Chen C T, Sette F, Ma Y and Modesti S 1990 *Phys. Rev.* B **42** 7262
[27] Imada S and Jo T 1990 *J. Phys. Soc. Japan* **59** 3358
[28] Thole B T, Carra P, Sette F and van der Laan G 1992 *Phys. Rev. Lett.* **68** 1943
[29] Carra P, Thole B T, Altarelli M and Wang X 1993 *Phys. Rev. Lett.* **70** 694
[30] Fischer P, Eimuller T, Schütz G, Guttmann P, Schmahl G, Pruegl K and Bayreuther G 1998 *J. Phys. D: Appl. Phys.* **31** 649
[31] Stöhr J, Wu Y, Hermsmeier B D, Samant M G, Harp G R, Koranda S, Dunham D and Tonner B P 1993 *Science* **259** 658
[32] Yamasaki A, Imada S, Utsunomiya H, Muro T, Saitoh Y, Negishi H, Sasaki M, Inoue M and Suga S 2001 *Physica* E **10** 387
[33] Yamasaki A, Imada S, Arai R, Utsunomiya H, Suga S, Muro T, Saitoh Y, Kanomata T and Ishida S 2002 *Phys. Rev.* B **65** 104410

[34] Kuch W, Frömter R, Gilles J, Hartmann D, Ziethen Ch, Schneider C M, Schönhense G, Swiech W and Kirschner J 1998 *Surf. Rev. Lett.* **5** 1241
[35] Negishi H, Koyano M, Inoue M, Sakakibara T and Goto T 1988 *J. Magn. Magn. Mater.* **74** 27
[36] Negishi H, Shoube A, Takahashi H, Ueda Y, Sasaki M and Inoue M 1987 *J. Magn. Magn. Mater.* **67** 179
[37] Imada S, Muro T, Shishidou T, Suga S, Maruyama H, Kobayashi K, Yamazaki H and Kanomata T 1999 *Phys. Rev.* B **59** 8752
[38] Kimura A *et al* 1993 *Japan. J. Appl. Phys.* **32** (Suppl.) 255
[39] Webster P J and Ziebeck K R A 1973 *J. Phys. Chem. Solids* **34** 1647
[40] Ziebeck K R A and Webster P J 1974 *J. Phys. Chem. Solids* **35** 1
[41] van Engen P G, Buschow K H J and Erman M 1983 *J. Magn. Magn. Mater.* **30** 374
[42] Brandão D E, Boff M A, Fraga G L F and Grandi T A 1993 *Phys. Status Solidi* b **176** K45
[43] Ishida S, Akazawa S, Kubo Y and Ishida J 1982 *J. Phys. F: Met. Phys.* **12** 1111
[44] Kimura A, Suga S, Shishidou T, Imada S, Muro T, Park S Y, Miyahara T, Kaneko T and Kanomata T 1997 *Phys. Rev.* B **56** 6021
[45] Endo K, Ooiwa K and Shinogi A 1992 *J. Magn. Magn. Mater.* **104–107** 2014
[46] Imada S *et al* 2000 *Japan. J. Appl. Phys.* **39** L585
[47] Imada S, Suga S, Kuch W and Kirschner J 2002 *Surf. Rev. Lett.* **9** 877
[48] Kuch W, Gilles J, Kang S S, Imada S, Suga S and Kirschner J 2000 *Phys. Rev.* B **62** 3824
[49] Hefferman S J, Chapman J N and McVitie S 1991 *J. Magn. Magn. Mater.* **95** 76
[50] Dürr H A, Guo Y G, van der Laan G, Lee J, Lauhoff G and Bland J A C 1997 *Science* **277** 213
[51] van Dijken S, Vollmer R, Poelsema B and Kirschner J 2000 *J. Magn. Magn. Mater.* **210** 316
[52] Fink R *et al* 1997 *J. Electron. Spectrosc. Relat. Phenom.* **84** 231
[53] Vogel J, Kuch W, Bonfim M, Camarero J, Pennec Y, Offi F, Fukumoto K, Kirschner J, Fontaine A and Pizzini S 2003 *Appl. Phys. Lett.* **82** 2299